Computational modeling and simulation of stenosis of the cerebral aqueduct due to brain tumor

Uzair Ul Haq, Ali Ahmed, Zartasha Mustansar, Arslan Shaukat, Sasa Cukovic, Faizan Nadeem, Saadia Talay, M. Junaid Iqbal Khan & Lee Margetts

Published online: 26 Apr 2022.

Submit your article to this journal ⬚

View related articles ⬚

View Crossmark data ⬚

Taylor & Francis
Taylor & Francis Group

🔓 OPEN ACCESS | Check for updates

Computational modeling and simulation of stenosis of the cerebral aqueduct due to brain tumor

Uzair Ul Haq[a], Ali Ahmed[b], Zartasha Mustansar [b], Arslan Shaukat[c], Sasa Cukovic[d], Faizan Nadeem[e], Saadia Talay[b], M. Junaid Iqbal Khan[f] and Lee Margetts[g]

[a]Department of Biomedical Engineering & Sciences, School of Mechanical & Manufacturing Engineering (SMME), National university of Sciences & Technology (NUST), Islamabad, Pakistan; [b]Department of Computational Engineering, School of Interdisciplinary Engineering and Sciences (SINES), National university of Sciences & Technology (NUST), Islamabad, Pakistan; [c]Department of Computer & Software Engineering, College of Electrical & Mechanical Engineering, National university of Sciences & Technology (NUST), Islamabad, Pakistan; [d]Institut für Biomechanik, Zürich, Switzerland; [e]Institute of Nuclear Medicine & Oncology Lahore (INMOL), Lahore, Pakistan; [f]Laboratory of Theoretical and Experimental Physics, Bahauddin Zakariya University, Multan, Pakistan; [g]Mechanical and Aeronautical Engineering Division L5, Department of Mechanical, Aerospace & Civil Engineering, The University of Manchester, Manchester, UK

ABSTRACT

Stenosis of the cerebral aqueduct (CA) is featured in many studies relating to elevated intracranial cerebral pressures. It also presents a challenging situation to clinicians. Compressive forces play a lead role in pathological situations such as the presence of tumors and hence can cause obstruction to the flow of cerebrospinal fluid (CSF). Because of this barrier, excessive retention of CSF in the ventricles can occur. This, in turn, can contribute to increased pressure gradients inside the cranium. Most of the numerical models in the literature are restricted to modeling the CSF flow by considering the ventricle walls as rigid material, although in reality they are deformable. This paper, therefore, addresses the same from a holistic perspective by taking into consideration the dynamics of the flexible characteristics of the ventricular wall. It adds novelty to this field by reconstructing anatomically realistic ventricular wall behavior. To do this, the authors aim to develop a computational model of stenosis of the CA due to a brain tumor by invoking a fluid–structure interaction (FSI) method. The proposed three-dimensional FSI model is simulated under two cases: first, simulation of the pre-stenosis case with no interaction of tumor forces and, secondly, a stenosis condition with dynamic interaction of tumor forces. Comparison of the forces with and without a tumor reveals a marked obstruction of CSF outflow after the third ventricle and CA. In addition, a drastic rise in CSF velocity from 21.2 mm/s in the pre-stenosis case to 54.1 mm/s in the stenosis case is observed, along with a net increase in deformation of 0.144 mm on the walls of the ventricle. This paper makes a significant contribution to brain simulation studies for pressure calculations, in which the presence of tumors is a major concern.

1. Introduction

Brain tumors can be benign or malignant. Compressive forces of the brain tumor may constrict the flow of cerebrospinal fluid (CSF), thereby causing stenosis of the cerebral aqueduct (CA). Likewise, during stenosis of the CA, obstructive hydrocephalus (which is a direct consequence of the constriction caused by brain tumor on the walls of the CA) can be seen as well. It is important to understand the core mechanisms of stenosis of the CA, and the nature, pathophysiology and biomechanics of the brain tumor and obstructive hydrocephalus, along with their relationship with each other. The study of stenosis of the CA primarily helps in understanding the increase in intracranial pressure (ICP) under particular circumstances. According to a survey conducted by CancerNet (2021), around 23,890 adults in the USA would be diagnosed with brain cancers in 2021; furthermore, every year about a million Americans are affected by hydrocephalus (Hydrocephalus Association, 2021). Stenosis of the CA is an important domain and a topical area for clinical discussion. Continuous monitoring of CSF pressure (and ICP) inside the cranium usually involves surgical interventions. The invasive mechanisms for clinically sensitive procedures are risky and cannot be performed as a matter of routine. However, a numerical model may overcome this clinical and practical limitation in a non-invasive manner. This would provide clinicians with better analytic methods to understand the interaction of the brain tumor with the walls of the CA and its effects, including stenosis, without surgical intervention.

CSF modeling enables us to exhibit fluid flow in the brain non-invasively. For this purpose, computational fluid dynamics (CFD) has been widely used to model fluid flows for biomedical applications. Many studies provide evidence for the same, including Jacobson et al. (1996), which used a simple cylinder to study the flow of CSF through the CA. This study suggests that a pressure difference of at least 1.1 Pa is required to drive the CSF from the CA. In another study (Fin & Grebe, 2003), a synchronized framework was proposed by considering two models, a cylindrical rigid wall model and an elastic wall model segmented from magnetic resonance imaging (MRI) data to study the flow of CSF in the CA. The spatial domain was digitized using the immersed boundary method (IBM) (Tu et al., 2018). The pulsatile velocity inlet boundary condition was used, and their results showed a pressure drop of 1.02 Pa and velocity of 30.20 mm/s for the cylindrical model. For the elastic wall model, a pressure drop of 2.91 Pa and velocity of 64.65 mm/s were observed. This drastic change in pressure when considering a deformable model of the ventricles is important. It raises concerns over assumptions used in the rigid wall model of ventricles. Linninger et al. (2005) proposed a two-dimensional (2D) rigid model of the human ventricular system (HVS), and reported a pressure drop of less than 2 Pa and velocity of 7.3 mm/s. In one of the extensive studies on CSF flow using the HVS (Howden et al., 2008), three-dimensional (3D) ventricles were segmented from MRI data and the CSF was treated as an incompressible Newtonian fluid (Gholampour, 2018). A pulsatile velocity inlet and zero-gauge pressure at the outlet boundary conditions were used. The maximum velocity and Reynolds number were found to be 11.38 mm/s and 15, respectively, in the CA. Similarly, Kurtcuoglu et al. (2005) provided a guided framework using a simplified geometry of the ventricles and compared their case with the simplified geometry of the stenosed CA. This study concluded that there was a change in pressure amplitudes and peak velocities relative to the case of stenosis. The study further concluded that under a stenosed CA, pressure amplitude in the lateral ventricles increased as the level of stenosis increased. (Jacobson et al. (1999) suggested that under mild stenosis, the pressure required to initiate CSF flow increased to 125 Pa. A conclusion of this work reveals an increase in the 'transmantle pressure' pivotally, even with little change in intraventricular pressures. Similarly, some of the framework of CFD modeling in other human organs, such as the airways and lungs, is provided in Koombua et al. (2008) and flow modeling through the cerebral vasculature is presented in Šutalo et al. (2014).

One relevant approach is fluid–structure interaction (FSI). Three papers are the most relevant in this context. First, Masoumi et al. (2010) presented a 2D FSI model of the ventricular system and a simulation of CSF flow inside the ventricle. A deformation of 0.006 mm on the walls of ventricles was reported. However, they used a 2D model. The second study was proposed by Gholampour (2018), who modeled a non-communicating hydrocephalus case and provided a 3D FSI model of the CSF using a simplified geometry of the subarachnoid space and ventricles. The aim was to look into model behavior of the hydrodynamics of the CSF under different situations. This study is relevant in terms of developing a 3D FSI model. The third is the study by Sweetman and Linninger (2011), in which a 3D FSI model was developed for studying the CSF flow inside the central nervous system (CNS). Using these last two studies, a similar 3D FSI model is developed for studying stenosis of the CA.

The literature gives a valuable insight into the study of stenosis of the CA. However, most of the studies have oversimplified the model. First, they assumed the rigid wall behavior of the ventricles and resorted to simple flow analysis, instead of considering the deformable nature of the ventricles. Second, when considering ventricular walls as rigid, one cannot model the effect of external forces, such as those originating from a brain tumor, on the behavior of intraventricular CSF flow. Hence, to study stenosis of the CA, these drawbacks need to be addressed. In brief, therefore, a different approach is needed for modeling stenosis of the CA, which forms the basis of our work.

The science of the present study relies on building a 3D FSI model which combines both the structural and fluid dynamics into a single framework. We have made an effort to show a complete understanding of the stenosed CA, by considering realistic conditions, including the deformable ventricular wall property and its relative fluid response. We have also incorporated the effect of pulsatility, as discussed above. Overall, the proposed model has the maximum fundamental features associated with it and can be applied in various cases apart from this specific example.

The remainder of the paper is organized as follows. Section 2 presents a description of the materials and methods, under which various procedural, numerical and simulation settings are discussed. Section 3 presents the results of the simulation. Section 4 discusses the results and limitations of the present study. Conclusions and directions for future work are presented in Section 5.
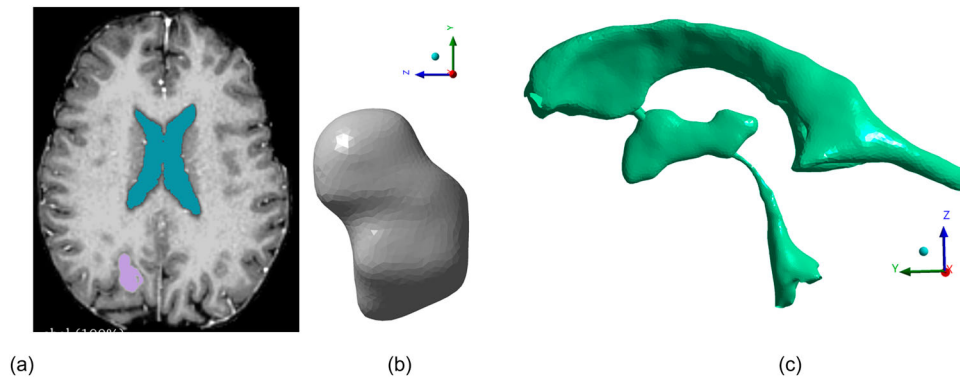
(a) (b) (c)

Figure 1. Magnetic resonance imaging data: (a) axial scan with tumor and ventricular regions highlighted; 3D reconstructions of (b) tumor and (c) ventricular geometry.

2. Materials and methods

2.1. Subject-specific MRI image and clinical characteristics

The MRI image used in this study is a T1 contrast-enhanced image acquired from a 1.5 Tesla machine. The spatial dimensions of the acquired MRI image are $512 \times 512 \times 288 \, \text{mm}^3$. The slice thickness in the z-dimension is approximately 0.6 mm. Ventricular and tumor geometries are segmented using a 3D slicer. The geometry is further refined using a Laplacian smoothing filter. Figure 1 shows an axial MRI scan and the segmented ventricle and tumor body.

2.2. Meshing of geometry and mesh independence test

A mesh independence study is performed to find the ideal grid size. Since the FSI technique is used, performing a mesh independence test on the fluid and structure domains separately gives a better indication of the converged solution. In the solid domain, SHELL 181 elements were used. This ensured a smaller computational load. A static structural solution was applied under a specified pressure and the maximum stress value was recorded. Following the mesh independence test, a grid size of 196,576 elements with a minimum element size of 0.3 mm was preferred, which was fine enough to capture all the physics in the simulation. Similarly, in the fluid domain, tetrahedral elements (SOLID 187) were used for meshing. A mesh independence study was carried out to identify the ideal grid size. The results confirmed that a mesh density of 1,144,379 elements with a minimum element size of 0.5 mm was good enough to capture all the important information regarding peak velocity changes in the simulation. Figure 2 shows the meshing of the geometry and Figure 3 shows the mesh independence study for both solid and fluid domains.
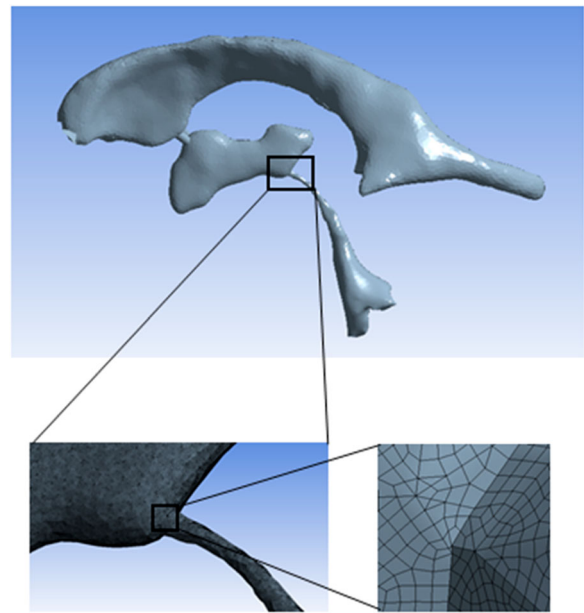

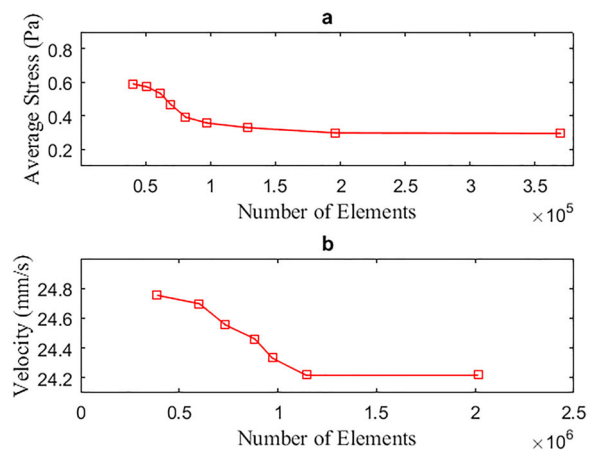**Figure 2.** Meshing of the three-dimensional model.

Figure 3. Grid independence study: (a) mesh independence for solid domain; (b) mesh independence for fluid domain.

Table 1. Material properties and boundary conditions.

Boundary conditions	Value	Reference
CSF density	1000 kg/m^3	Masoumi et al. (2010)
CSF viscosity	0.001003 Ns/m^2	Howden et al. (2008)
Bulk mass flow	6.25×10^{-6} kg/s	Masoumi et al. (2010)
Pressure outlet	0 Pa	Howden et al. (2008)
Modulus of elasticity	30 kPa	Masoumi et al. (2010)
Ventricular tissue density	1000 kg/m^3	Masoumi et al. (2010)
Poisson's ratio	0.49	Masoumi et al. (2010)

2.3. Material properties: solid domain

The choice of material properties for ventricular geometry was the most critical part of this study since it is responsible for the overall behavior of the model. The density of the ventricular geometry and the Poisson ratio were taken as 1000 kg/m^3 and 0.49, respectively (Masoumi et al., 2010). One thing that must be noted here is that, in the literature, the ventricular geometry is largely modeled as elastic when it is studied in an isolated environment. Masoumi et al. (2010) report the modulus of elasticity for ventricular geometry as being in the range of 10–30 kPa. Furthermore, it is well established that the ventricular geometry is a soft-tissue geometry and can have anisotropic or non-homogeneous properties, or may have a non-elastic nature when taken together with the brain tissue (Yang et al., 2014). For instance, Sweetman and Linninger (2011 modeled the subarachnoid FSI boundary as neo-Hokean. However, the true biomechanical nature of ventricles is still debatable and is subject to the availability of data from *in vivo* studies. The prevailing data in the literature suggest that the ventricles gain their properties, such as viscoelasticity, from the surrounding tissues (Yang et al., 2014). Since we are considering the ventricles in an isolated environment, a linearized model from the literature (Masoumi et al., 2010) was preferred. Table 1 shows the material properties.

2.4. Governing equations

The numerical model on the fluid side consists of solving the equations of conservation of mass and momentum (Batchelor, 2000) given below:

$$\Delta \cdot (\rho \cdot \vec{V}) = 0 \tag{1}$$

$$P\frac{\partial \vec{V}}{\partial t} + \rho(\vec{V} \cdot \nabla)\vec{V} = -\nabla P + \tau\rho + \mu\nabla^2\vec{V} \tag{2}$$

where ρ is the density of the fluid, v is the velocity of the fluid, ∇ is the gradient operator, $\rho\frac{\partial \vec{v}}{\partial t}$ is the local acceleration of fluid particles, $\rho(\vec{v}.\nabla)\vec{v}$ is the convective acceleration, ∇P is the pressure gradient, $\tau\rho$ are body forces, and $\mu\nabla^2\vec{v}$ is the viscous term, which resists the motion of the fluid particles.

Solving Equations (1) and (2) requires spatial and temporal discretization together with pressure–velocity coupling schemes. This method can be used to interpolate pressures at the faces of a control volume. A pressure-based solver is used with pressure implicit with splitting of operator (PISO) coupling. For spatial discretization, second order pressure was used, and for momentum, second order upwind was used. For gradient discretization, the least square cell-based method was used. Implicit formulation is used in discretizing equations. An implicit time marching scheme was employed, using the second order backward Euler derivative formulation.

The governing equations relevant for the structural mechanics part are as follows (Masoumi et al., 2010):

$$\{\sigma\} = E\{\varepsilon\} \tag{3}$$

where E is the stiffness matrix, σ is the stress vector, and ε are the strains. The linear stress–strain law is applied to achieve deformation on the body. The Newmark integration scheme is used to solve nonlinear equations and therefore an implicit solver is needed to move towards a solution. The implicit time marching scheme is used together with the Newton–Raphson method for loads and displacement convergence. The Newton–Raphson equation is given as follows (Fluent, A.N.S.Y.S., 2011):

$$X_{N+1} = X_N - \frac{F(X_N)}{F'(X_N)} \tag{4}$$

Equation (4) is used to converge forces, moments and displacements at each timestep, which works on the principle that the energy added as a result of the external loads must eventually balance the energy induced by the reaction forces. The governing condition for FSI coupling is the kinematic coupling condition (Bodnár et al., 2014) in which a no-slip condition with the fluid and structure interface was followed. The FSI equations for the kinematic coupling at the interface Γ are given as follows (Bodnár et al., 2014):

$$u_\Gamma(t) = d_\Gamma^F(t) \tag{5}$$

$$u_\Gamma'(t) = v_\Gamma(t) \tag{6}$$

$$u_\Gamma''(t) = v_\Gamma(t) \tag{7}$$

where $d_\Gamma^F(t)$ is the displacement of the fluid mesh at the interface. The dynamic coupling is given by (Bodnár et al., 2014):

$$\sigma^f.n^f + \sigma^s n^s = 0 \tag{8}$$

where σ^f is the stress tensor on the fluid side, n^i is the normal vector, and σ^s is the stress tensor on the solid side. The product $\sigma^i.n^i$ is called the traction vector. Owing to
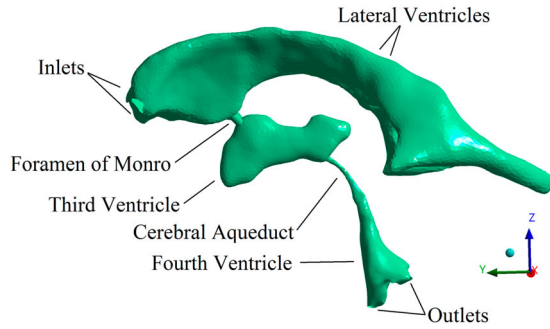
Figure 4. Boundary conditions. All surfaces except the inlets and outlets were part of the fluid–structure interaction interface.

displacements, dynamic meshing adaptability is needed so that the moving cells on the fluid and solid side can be remeshed correctly, thereby preserving the shape quality. In ANSYS FLUENT, diffusion-based smoothing was used, with the diffusion parameter equal to 2.

2.5. Boundary conditions and tumor growth modeling

The boundary conditions were selected so as to make the model as realistic as possible. The model consisted of two inlets and two outlets, each of 3 mm^2 diameter. These inlets were defined in the later ventricles, whereas outlets were defined in the fourth ventricle. The choroid plexus lines the inside of the walls of ventricles and, in reality, the inside walls behave as a source of CSF, whereas in this study, inlets were defined at particular points (Figure 4), which is consistent with previous studies (Howden et al., 2008; Masoumi et al., 2010; Sweetman & Linninger, 2011). This is because of the behavior of CSF fluid flow is largely a creeping flow (Howden et al., 2008; Masoumi et al., 2010). The flow is consequently assumed to be in the laminar region throughout (Howden et al., 2008). Therefore, defining the entire inside walls of lateral ventricles as inlets has no ultimate bearing on the velocity profile across the CA.

On the fluid side, the mass flow inlet boundary condition with bulk production of 500 ml/day (or 6.25×10^{-6} kg/s) was used to mimic the real scenario of CSF flow (Tu et al., 2018). At the outlet, a static pressure of 0 Pa was defined (Gholampour, 2018). CSF behaves very similarly to water (Bodnár et al., 2014), with a density of about 1000 kg/m^3 and a constant viscosity of 0.00103 Pa.s. The protein content has very limited and negligible effect (Bodnár et al., 2014). CSF was, therefore, treated as a Newtonian fluid. A Newtonian fluid is usually described by Newton's law of viscosity, presented in mathematical form as (Bodnár et al., 2014):
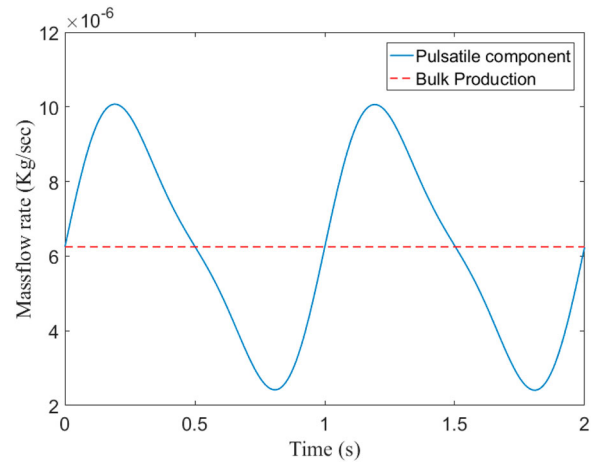
$$\sigma = \mu \frac{du}{dy} \qquad (9)$$

Figure 5. Pulsatile component of cerebrospinal fluid (in mass flow rate) determined using Equation (10).

where σ is the shear stress, du/dy is the gradient of shear strain, and μ is the dynamic viscosity constant.

Equation (9) suggests that if shear stress is directly proportional to the rate of shear strain, then a fluid will behave as a Newtonian fluid. This means that the shear stress along the walls will be maximum and the fluid which is in contact with the medium has zero velocity/strain relative to the wall. This is, therefore, a no-slip condition. The shear strain along the wall will be zero.

To add more value to this study, a novel schematic boundary condition was employed, using CSF pulsatility induced during the cardiac cycle and its effect on stenosis of the CA. The pulsatile component is ideally a linear combination of sinusoidal harmonics, given as (Wagshul et al., 2006):

$$\begin{aligned} \text{Volumetric flow rate } (T) = {} & \text{Bulk production} \\ & + A\sin(Wt + \alpha) \\ & + B\sin(2wt + \beta) \end{aligned} \qquad (10)$$

In Equation (10), bulk production, as noted above, is approximately equal to 0.3 ml/min (6.25×10^{-6} kg/s), A is equal to 0.21 ml/min (3.5×10^{-6}), and B is the part of second harmonic and is taken to have an amplitude of 0.05 ml/min (Wagshul et al., 2006). The carotid artery, which takes blood away from the heart, has zero phase difference (Wagshul et al., 2006), similarly to the CSF flow-rate phase at the C2 vertebral column level (Wagshul et al., 2006). However, CSF velocity in the CA has a phase difference. α and β were assumed to be zero. The pulsatile component was plotted against time and is given in Figure 5.

Regarding the external loading which came from the tumor, it is obvious that the initial tumor size needs to grow along the temporal spectrum so that the loading
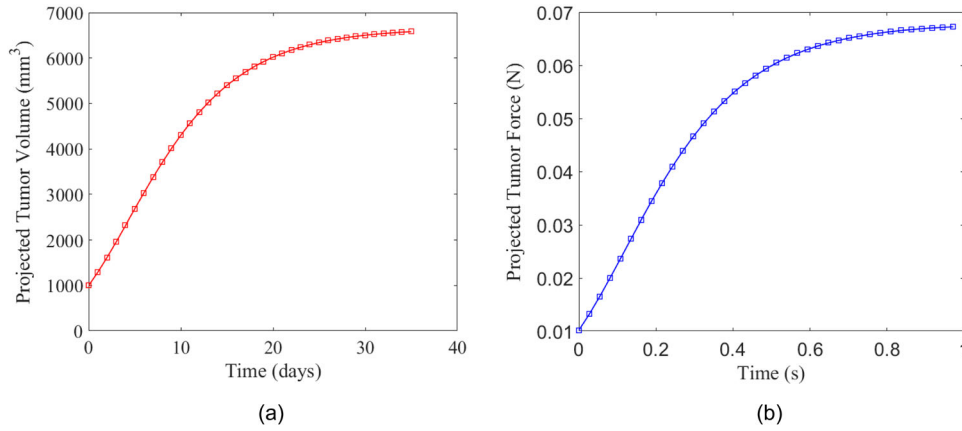
Figure 6. Tumor growth modeling: (a) tumor grown for 35 days using the Gompertz model; (b) associated force in 0–1 timescale.

conditions can become dynamic in nature. To predict the growth of the tumor, the Gompertz mathematical model is used, which is one of the widely used models to extrapolate tumor cells based on the initial tumor volume (Benzekry et al., 2014). The model has the solution of the form given by:

$$\text{Volume}(T) = V(0)e^{\frac{\alpha}{\beta}(1-E^{-\beta t})} \tag{11}$$

where $V(0)$ is the initial tumor volume, α and β are the initial proliferation rate and the exponential decay constants, which have values of 0.279 and 0.1470 (Murphy et al., 2016), and t is the time in days.

Figure 6(a) shows the growth of tumor volume over time. From the growth of tumor volume, body forces can be calculated. Body forces can be thought of as forces acting on the entire volume of a body, such as forces due to gravity. These forces are basically the weight of the body and can be given as:

$$F = \int \rho g dv \tag{12}$$

where F is the body force, ρ is the density of the tumor mass, which is taken to be 1040 kg/m^3 (Yang et al., 2014), g is acceleration due to gravity (9.81 m/s^2), and dv is the volume differential element. Figure 6(b) shows the plot of force versus time, determined using Equation (12). This force is used in Equation (2) as the body force.

2.6. Fluid–solid interface

To set up the simulation, solid and fluid domains were set up separately; CSF was referred as the fluid domain and the ventricular walls as the solid domain. The fluid–solid interface boundary was defined by creating a surface Ωs, such that it acts as a coupling, where two variables (forces and displacements) were transferred at each timestep. The complete ventricular surface, except for inlets and outlets, was defined as an FSI surface.

3. Results

ANSYS software was used for the model simulation. This software provides a system coupling toolbox through which structural and fluid solvers can be united via a strong coupling method (having the same timestep sizes) so that data transfer occurs at the same timestep between the solvers. The timestep size used in this study is taken to be 0.01 s. The results are presented below with regard to various important parameters.

3.1. Model validation

Segmented tumor and ventricles from the MRI data points were validated as well. A comparison of the segmented and ground truth the volumes (provided by the radiologist) is provided in Table 2. The percentage errors with reference to the ground truths for the ventricle and tumor are 4.18% and 3.93%, which are acceptable since large deviations have been eliminated. Hence, in terms of geometry, the model is largely validated within generally acceptable limits of 5% error.

3.2. CSF flow field and Reynolds number under stenosis of CA

The velocity field is an important parameter in CSF modeling. The CSF peak velocity always occurs in the cross-section of the CA owing to the narrow pathway. The simulation results are presented for two cases.

The first case pertains to the FSI simulation of the ventricular body with no interaction of tumor forces. Figure 7 shows vector plots of velocity in the third and fourth ventricle at different timesteps for cases where the tumor forces act on the walls of the CA, resulting in different levels of stenosis. Figure 7(a) shows the case when the tumor forces are minimum and 10% stenosis in the CA is observed. Figure 7(b) and (c) is the second

Table 2. Ventricular and tumor segmentation validation.

Specimen	Ventricular volume			Tumor volume		
	Segmented volume (ml)	Ground truth volume (ml)	Percentage error	Segmented volume (mm^3)	Ground truth volume (mm^3)	Percentage error (%)
MRI image	25.32	24.32	4.18	997.29	959.51	3.93

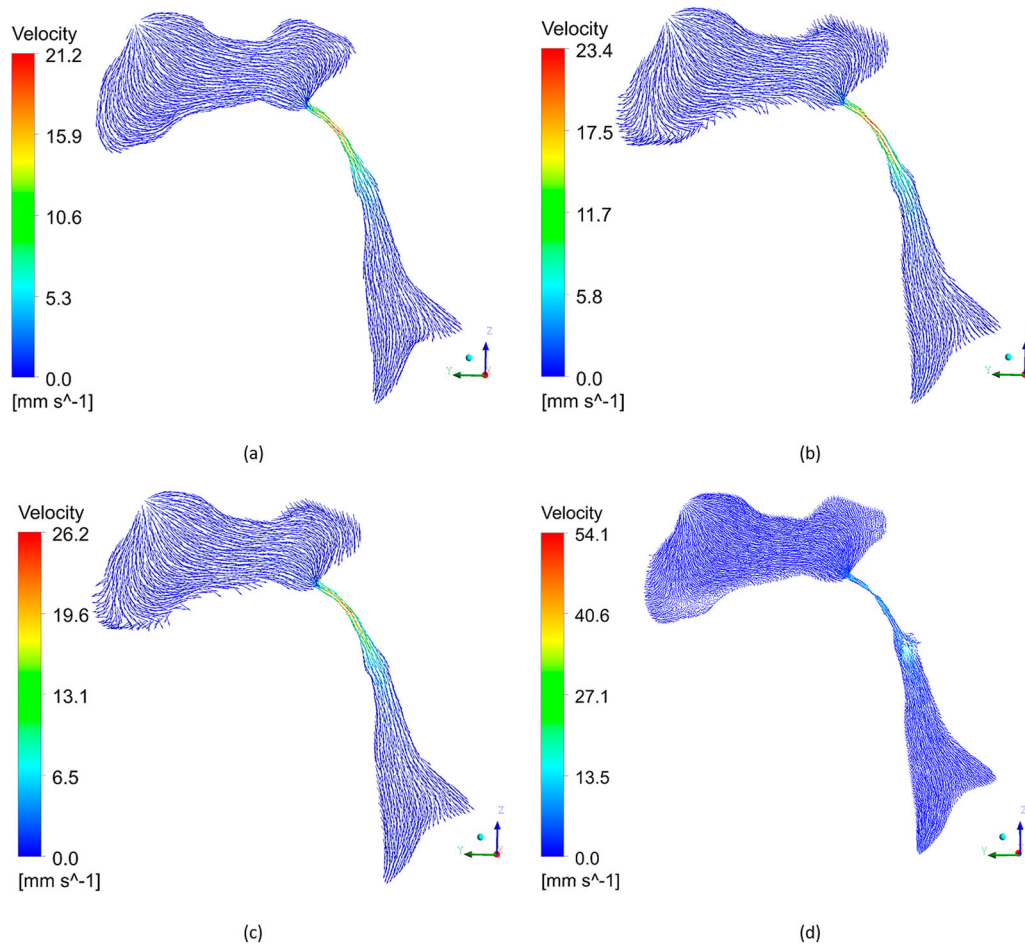Note: MRI = magnetic resonance imaging.

Figure 7. (a) Maximum velocity when no external force acts; (b) velocity in cerebral aqueduct (CA) at timestep 0.1 s; (c) velocity in CA at timestep 0.5 s; (d) velocity in CA at 0.75 s, showing considerable constriction in the CA where the velocity vectors start to distort.

case which shows the steady rise in the CSF velocity due to the narrowing of the pathway because of increasing tumor forces. However, after some time, the tumor forces increase to a greater magnitude, constricting further the pathway of the CA. This constriction corresponds to the maximum stenosis of the CA, as a result of which the velocity rises drastically to 54.1 mm/s, showing that the duct has deformed considerably relative to the previous stenosis levels. Figure 7(d), shows that the velocity vectors at the point of constriction have started to change direction as well. This suggests that the deformable property of the ventricle should not be overlooked because it has a visible effect on the biomechanics of the system.

Another useful parameter to gauge the dynamics of CSF under the scenario of stenosis of the CA was to determine the Reynolds number of the flow. The Reynolds number is an important parameter which signifies the transition of flow from laminar to turbulent. It is given by:

$$Re = \frac{\rho \vartheta D}{\mu} \qquad (13)$$

From Equation (13), the Reynolds number is directly proportional to the velocity, which suggests that as the flow velocity increases, so does the Reynolds number. Flow in the lateral ventricles is in order of 10^{-3} mm/s,

which clearly shows characteristics of creeping flow. Consequently, in terms of the Reynolds number in the lateral ventricles, there is no noticeable effect. However, the flow velocity in the CA changes abruptly and so does the Reynolds number. Whereas for the case presented in Figure 7(a), the Reynolds number is found to be 38.5, for the case presented in Figure 7(d), where 75% stenosis is observed, it rises to 110. The maximum Reynolds number is found to be 110, which suggests that the CSF flow in the CA is overall laminar. However, a stenosed CA represents a complex situation in which the flow profile, velocity and Reynolds number change significantly and may cause clinical complications.

3.3. Ventricular wall pressures

Ventricles are cavities containing CSF fluid. CSF pressure on the walls of ventricles is an important fluid dynamic variable which drives flow through any media via pressure differences. From Figure 1, it can be seen that there are four ventricles, which are cavities interconnected through different channels such as the foramen of Monro and the CA. Among them, the lateral ventricles are largest in terms of volume and space, and the rest are smaller than the lateral ventricles. Hence, the pressure gradient and amplitude ought to be larger in the lateral ventricles. A larger pressure variation also determines the transmantle pressure. The transmantle pressure is the net pressure gradient across the parenchyma all the way to the subarachnoid space. If transmantle pressures are high owing to high intraventricular pressure, then the patient may experience elevated ICP. Simulation results determine whether transmantle pressures increase in the case of stenosis of the CA compared to that of the non-stenosed duct, which would also show a corresponding difference in cases with elevated ICP.

Figure 8 shows the results of the pressure field distribution on the walls of the ventricles. Figure 8(a) pertains to the case of a healthy brain where no tumor is present. In this case, a maximum pressure of 2.5 Pa is observed. It is also observed that the pressure variations in large cavities such as the lateral ventricles were found to be spatially uniform. This is perhaps because of their large size. Pressure drops of 0.2 and 1.7 Pa are found across the third ventricle and the CA. A large pressure drop across the CA is observed owing to the narrow pathway resulting in a greater pressure drop.

Figure 8(b) pertains to a tumor-specific case, where the pressure field is reported for a stenosed CA. In this case, a higher pressure in the lateral ventricles is observed owing to decreased outflow towards the fourth ventricle. The maximum pressure of 5.4 Pa is found in the lateral ventricles, with a pressure drop of 0.8 Pa in the third ventricle. The pressures in the CA present a unique case. A stenosed duct is practically a duct that is squeezed to a point where there is no outflow. Hence, beyond that point no fluid enters, which makes the pressure in that section drop below the surrounding pressures. This confirms that under a stenosed CA, the pressure in the CA and the fourth ventricle drops significantly, and the pressure in the lateral ventricles increases, indicating distension of the lateral ventricles.

Figure 8(c) shows the wall shears on the walls of the CA and fourth ventricle. Wall shear stress is an additional feature which contributes towards the valuable analysis in this study. In a stenosed CA, force acts on the walls of the CA. This causes the fluid layers to abruptly overlap with each other in the localized region, causing the velocity to change significantly, resulting in high shear stresses. A non-stenosed CA does not give high wall shear stresses (having stresses in the order of 10^{-2} Pa), which suggests that CSF flow normally has a laminar profile. However, under the influence of a tumor, the shear stress rises to 25 Pa. This additional parameter makes a significant contribution to our understanding of flow mechanics in the presence of a tumor.

3.4. Deformation on walls of ventricles

Since the walls of the ventricles have been modeled as elastic, their deformable character results in deformation. Figure 9 shows the deformation field obtained on the walls of ventricles in two cases. Case 1 (Figure 9a) pertains to the case of a non-stenosed CA. It shows a usual and nominal deformation of 2.0 μm. Case 2 (Figure 9b) shows a tumor-specific case. In this particular case, a drastic increment in deformation of the lateral ventricles of 0.146 mm is observed.

This deformation shows that once the CSF flow is obstructed considerably, the pressure in the lateral ventricles increases and deforms the lateral ventricles. It also creates a requisite compliance for the excessive retention of CSF fluid, which cannot flow towards the fourth ventricles owing to constriction. Since this particular case has not been modeled, even in 2D, the values presented herein can only be interpreted intuitively.

3.5. Effect of considering CSF pulsatility on stenosis of CA

The pulsatile component of CSF is induced owing to the blood flow in the cerebral vasculature during a cardiac cycle. The pulsatile mass flow inlet is provided using Equation (10). Figure 10 shows the simulation results due to the cardiac cycle on the flow of CSF in the ventricles.
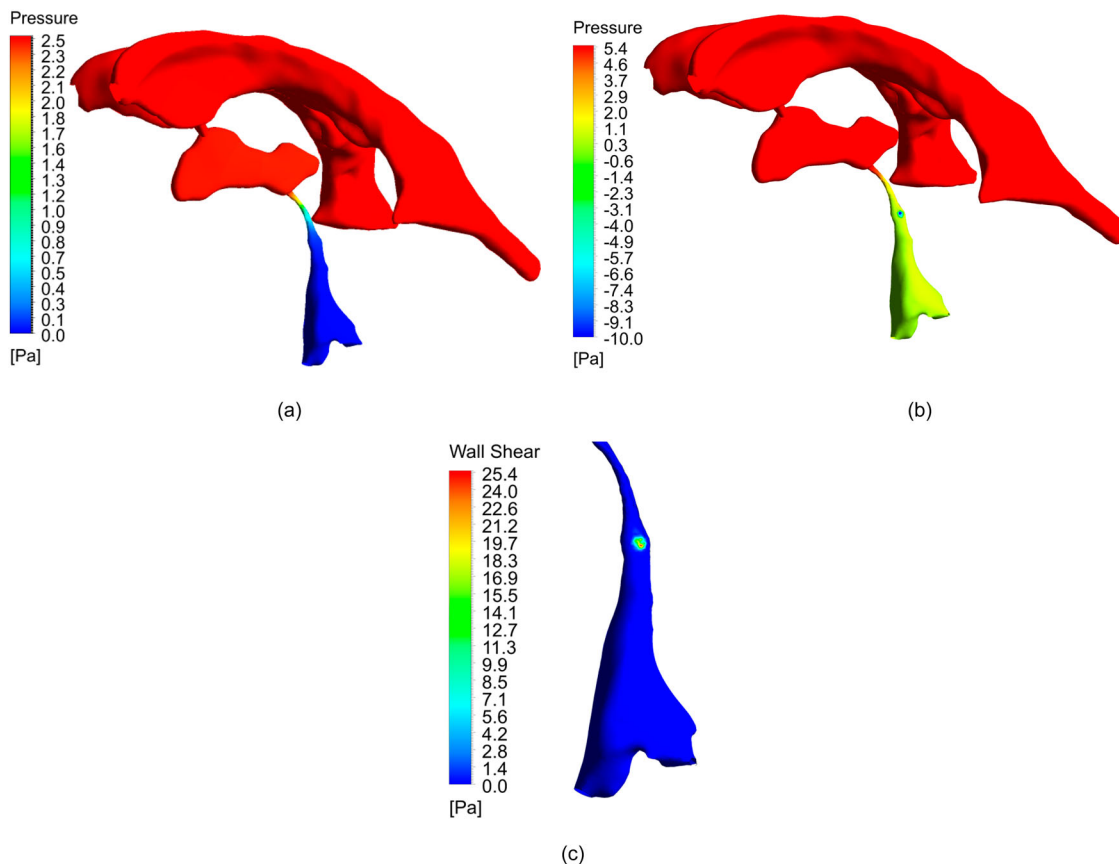
Figure 8. Pressures on the walls of ventricles: (a) pressure distribution on the walls of ventricles when no tumor force acts; (b) pressures on the walls of ventricles when the tumor force acts; (c) wall shear created as a result of tumor force.
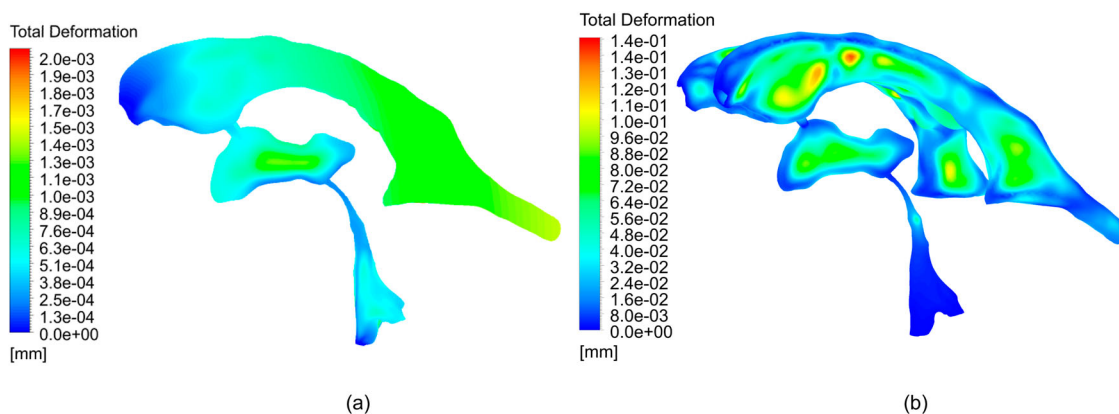

Figure 9. Deformation distribution on the walls of ventricles: (a) deformation when no tumor is acting; (b) increased deformation due to the action of tumor force.

Figure 10 suggests that the pulsatile component of CSF has a drastic influence on the CSF velocity, which rises to 58.21 mm/s. The motion of the cerebral vasculature pushing and driving CSF flow creates additional force, which produces motion of the CSF in the ventricles. Deformation observed on the walls of the ventricles increases when considering the pulsatile nature of CSF. As stated above, the deformation observed on the walls of ventricles under the stenosed CA is 0.146 mm; when

accommodating the pulsatile nature, the deformation increases to 0.40 mm.

4. Discussion

This study presents a 3D FSI model of stenosis of the CA due to the compressive forces of a brain tumor. Our work aims to provide a basic framework from which any
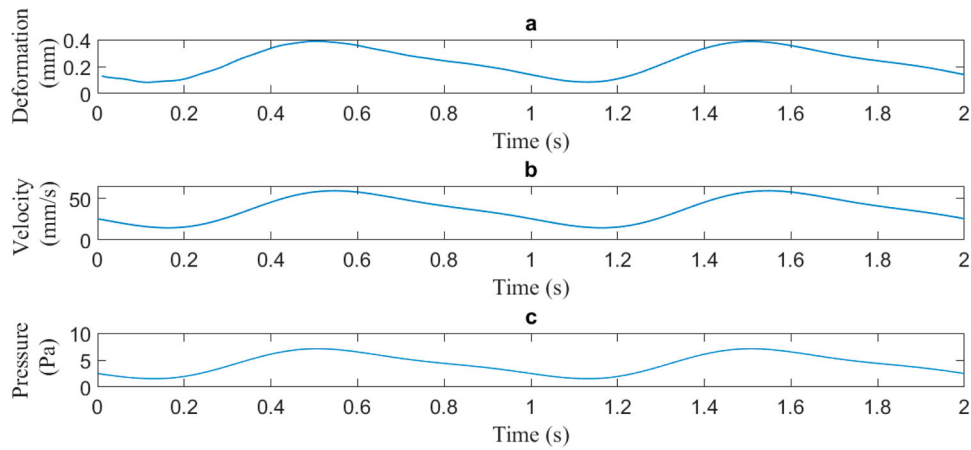
Figure 10. Graphs of (a) deformation on walls of ventricles; (b) velocity in cerebral aqueduct; (c) maximum pressure variation in lateral ventricles.

Table 3. Comparison of the results of the proposed method with previous fluid–structure interaction-based papers (with 25% stenosis, velocity increased by 30%).

Study	Velocity (mm/s) in CA	Pressure drop (Pa)	Deformation (mm)
Jacobson et al. (1996)	28	< 1.1 for CA	Walls modeled as rigid
Fin and Grebe (2003)	64.65	2.91 for elastic wall model for CA	Implemented flexible cylindrical wall model of CA and obtained 0.61 mm deformation
Linninger et al. (2005)	25.8/−21.7	2 in CA	No deformation reported; however, net increase in ventricular volume of 4.5% is reported
Kurtcuoglu et al. (2005)	With 25% stenosis, velocity increased by 30%	With 25% stenosis, intraventricular pressure increased by 8.9%	No deformation reported
Howden et al. (2008)	11.38	1.14	Walls modeled as rigid
Masoumi et al. (2010)	8/−6	< 2	Normal CSF–ventricular interaction: 0.006
Proposed method	Without tumor interaction: 21.2; stenosis of CA: 54.1	Without tumor interaction: 2.5; stenosis of CA: 5.4	Without tumor interaction: 0.002 ; stenosis of CA: 0.146

Note: CA = cerebral aqueduct.

ventricle–CSF interaction can be studied. For better visualization, two cases are simulated, with and without the interaction of a tumor. This comparison allows us to visualize differences between the two conditions. For these two cases, various flow parameters, such as CSF velocity, pressures (transmantle pressures), Reynolds number and deformation values, are calculated. The role of CSF pulsatility is also catered for in the proposed model to allow realistic model interpretation. The results of this study show that the impact of the deformable nature of the ventricle wall is significant. CSF velocity and transmantle pressures increase significantly in the obstruction phase, from 21.2 mm/s in the pre-stenosis case to 54.1 mm/s in the stenosed case, accompanied by a net deformation increase of 0.144 mm on the walls of the ventricle. These

results are benchmarked against the results presented in the literature.

It is important to discuss here how the results were validated. Validation of results was carried out via two independent sources. First, we validated our results with the past models of FSI presenting case studies of CSF flow parameters. The second source of validation was phase-contrast magnetic resonance imaging (PC-MRI) studies, taken from the literature, which provide experimental results for CSF flow parameters. Table 3 provides the results of the present case and compares them with previous FSI-based papers, and Table 4 provides a comparison of PC-MRI studies reported in the literature. In Table 3, our study is compared against previous papers of simple CFD modeling or FSI papers, by Jacobson et al. (1996),

Table 4. Comparison of the results of the proposed method with phase-contrast magnetic resonance imaging (PC-MRI) studies reported in the literature.

PC-MRI study	Stroke volume (ml/beat) ($\pm$ SD)	Peak velocity craniocaudal (cm/s) ($\pm$ SD)
Abbey et al. (2009)	0.017 $\pm$ 0.010	3.24 $\pm$ 1.08
Algin et al. (2010)	0.039 $\pm$ 0.039	4.78 $\pm$ 2.48
Lee et al. (2004)	0.02 $\pm$ 0.0125	3.39 $\pm$ 1.61
Proposed method	0.006 $\pm$ 0.01	Without tumor: 2.1; with tumor: 5.4

Fin and Grebe (2003), Linninger et al. (2005), Kurtcuoglu et al. (2005), Howden et al. (2008) and Masoumi et al. (2010). The results from our proposed model are better in that our model presents a 3D FSI model and also presents a better explanation and improved characterization of the flexible character of the ventricles than the study by Masoumi et al. (2010), whereas the studies by Jacobson et al. (1996), Fin and Grebe (2003), Linninger et al. (2005), Kurtcuoglu et al. (2005) and Howden et al. (2008) are limited as they consider the ventricular surface as rigid. Table 4 presents some basic PC-MRI studies on CSF volume and velocities, as an additional parameter by which to correlate and validate the velocities. These studies are by Abbey et al. (2009), Algin et al. (2010) and Lee et al. (2004). Accurate depiction of velocity for a particular case may not be available, but these results do present an indirect correlation or validation. Furthermore, for various levels of stenosis (10–75%), graphs are plotted of velocity, pressure and Reynolds number, which are provided in Figure 10. This is done to better visualize the changing character of these parameters at different percentages of stenosis.

From a theoretical and practical perspective, we conclude that various flow parameters, and the magnitude and location of tumor forces, affect the outcome. One important parameter is transmantle pressure. The higher the transmantle pressure, the higher the distension/deformation on the ventricular body. This has also been alluded to in previous research (Holmlund, 2019; Masoumi et al., 2010). CSF pulsatility amplifies and increases the transmantle pressure. Hence, another conclusion is the physiological role and importance of pulsatility in 3D FSI calculations of CSF in intraventricular and intracranial systems.

4.1. Limitations

There are limitations associated with this study too, which need to be discussed here. The first limitation is the factor of gravity. Gravity affects the flow of fluids in general. However, if the flow is single phase and the fluid is incompressible (as is CSF in the proposed case), then gravity has little effect on the flow field because when there is no net change in density, the fluid forces will be exactly the same and will counteract the gravitational forces.

The second is the factor of slight pulsations caused by respiration (similar to cardiac-induced pulsations). In cases where breathing is normal, CSF movement is little influenced by normal thoracic breathing (Takizawa et al., 2017); however, if deep excursions and abdominal breathing are considered, then it can be presumed that they may induce some effect on CSF flow (Aktas et al., 2019).

The third limitation, which would have a larger effect but was not considered in this study, is that we have mainly focused on the tumor forces due to the solid core contributing body forces, and have neglected the fluid component. Although the tumor's solid core is essentially made up of extracellular matrix and collagen fibers, which make by far the largest contribution towards tumor forces and can be assumed to approximate around this force, considering fluid forces may improve the model. This would also help in understanding behavior when the growing extracellular matrix has either ruptured (due to hydrostatic forces) or created a cerebral edema in its vicinity. Hence, if edema is present, it would be advisable to consider the effect of fluid hydrostatic pressure.

Fourth, we have applied tumor forces on the walls of ventricles. This simplification allows us to understand the biomechanical behavior and physiology of stenosis of the CA. This approach is best suited to considering intraventricular tumors. However, if the tumor is at any other location, then either the interaction of brain parenchyma needs to be considered or a transformation matrix is needed to find the transmission factor by which forces are either reduced or increased as they travel through the brain parenchyma. Furthermore, a force field or body forces may be enough to determine the major effect of the tumor on the walls of the CA. However, sometimes a stress field is also needed if interaction with brain parenchyma is considered.

Lastly, the CSF biomechanical model is constructed by segmenting anatomically realistic brain ventricles. We did not consider the effect of the subarachnoid space, where 75% of CSF volume is usually found. The purpose of not considering the subarachnoid space in this study pertains to the fact that the biomechanical properties, flow parametrization and transmantle pressure distributions are largely driven or influenced by changes in the biomechanical behavior of CSF in the ventricular regions, apart from the CA. For instance, obstructive hydrocephalus is caused by stenosis of the CA, thereby increasing ICP; changes in CSF velocity in the subarachnoid

space are negligible because it is a large cavity, and thus creeping flow dominates. Therefore, when analyzing the biomechanical properties of CSF, another dimension of studying the behavior of CSF inside the ventricles may be a useful parameter.

Apart from the discussion presented above, it is important to mention that this particular study is unique in addressing a broader application of tumor and hydrocephalus in brain dynamics. More precisely, this study makes the following important contributions:

1. First, this study documents the relevant interaction of ventricles, CSF and a brain mass (tumor, in this case) through the FSI scheme (two-way, in this case) where both solid and liquid matter interact in real time. This interaction was necessary to model (and calculate) and thus establish and develop a mathematical relationship/finite element model to take into account (in future) other brain layers, such as gray matter, white matter, skull and, in essence, the entire brain case, to make it more realistic.
2. Second, tumor growth is assumed to follow a mathematical modeling scheme (the Gompertz model, in this case). We can substitute such a real-time modeling scheme for such patients, subject to the availability of data. The pipeline and a model are devised in this paper to provide an essential framework to model various cases.
3. Third, the mentioned case relates to hydrocephalus because it narrates to the modeling of obstructive hydrocephalus, which is also (among others) diagnosed in cases; concerning stenosis of the aqueduct due to brain tumor, such as tumors found in third or fourth ventricle. In obstructive hydrocephalus, there is an extreme blockage of CSF flow, which ultimately affects the overall pressure dynamics of the skull. Hence, the study addresses the whole dynamics of the brain, with mass/tumor intervention.

5. Conclusion and future work

This paper is, to the best of our knowledge, the first to model stenosis of the CA under the influence of a brain tumor using FSI modeling. Our work shows that by using image informatics coupled with FSI modeling, the underlying ventricular–CSF interaction can be well established and understood. Furthermore, the proposed model is not restricted to the particular case at hand but can also be extended to other cases where CSF–ventricular interaction is under consideration. For future work, we hope to extend our proposed work and include three particular aspects in our model: first, the interaction between the subarachnoid space and brain parenchyma, which

will define a complete intracranial environment during the CSF–ventricular interaction; second, the role of fluid forces of the tumor, which may influence the outcome, especially if they are accompanied by cerebral edema; and third, the role of the blood–brain barrier and cerebral vasculature, to obtain more accurate and closer representation of the pulsatile nature of CSF.

Geolocation information

This study was conducted in Islamabad, Pakistan.

Disclosure statement

No potential conflict of interest was reported by the authors.

Authors' contributions

M. Uzair and A. Ahmed worked on the methods, experimentation and analytical aspects of paper. Z. Mustansar worked on reviewing this manuscript, acquired funding for this research and supervised the entire study. Z. Mustansar and A. Shaukat worked on the organization of the paper. F. Nadeem provided MRI datasets for this research. J. Iqbal Khan contributed to the material properties and behavior of the models. S. Cukovic and L. Margetts reviewed the manuscript. S. Talay participated in formatting the manuscript.

ORCID

Zartasha Mustansar 🔘 http://orcid.org/0000-0002-2327-7577

References

Abbey, P., Singh, P., Khandelwal, N., & Mukherjee, K. K. (2009). Shunt surgery effects on cerebrospinal fluid flow across the aqueduct of Sylvius in patients with communicating hydrocephalus. *Journal of Clinical Neuroscience*, *16*(4), 514–518. https://doi.org/10.1016/j.jocn.2008.05.009

Aktas, G., Kollmeier, J. M., Joseph, A. A., Merboldt, K.-D., Ludwig, H.-C., Gärtner, J., Frahm, J., & Dreha-Kulaczewski, S. (2019). Spinal CSF flow in response to forced thoracic and abdominal respiration. *Fluids and Barriers of the CNS*, *16*(1), 1–8. https://doi.org/10.1186/s12987-019-0130-0

Algin, O. M. D., Hakyemez, B. M. D., & Parlak, M. P. M. D. (2010). The efficiency of PC-MRI in diagnosis of normal pressure hydrocephalus and prediction of shunt response. *Academic Radiology*, *17*(2), 181–187. https://doi.org/10.1016/j.acra.2009.08.011

Batchelor, G. K. (2000). *An introduction to fluid dynamics*. Cambridge University Press. https://doi.org/10.1017/CBO9780511800955

Benzekry, S., Lamont, C., Beheshti, A., Tracz, A., Ebos, J. M. L., Hlatky, L., & Hahnfeldt, P. (2014). Classical mathematical models for description and prediction of experimental tumor growth. *PLoS Computational Biology*, *10*(8), e1003800–e1003800. https://doi.org/10.1371/journal.pcbi.1003800

Bodnár, T., Galdi, G. P., & Nečasová, S. (2014). *Fluid-structure interaction and biomedical applications*. Springer Basel. https://go.exlibris.link/NXpJ3Nrk

Cancer.Net. (2021). Brain tumor: statistics. https://www.cancer.net/cancer-types/brain-tumor/statistics

Fin, L., & Grebe, R. (2003). Three dimensional modeling of the cerebrospinal fluid dynamics and brain interactions in the aqueduct of Sylvius. *Computer Methods in Biomechanics and Biomedical Engineering*, *6*(3), 163–170. https://doi.org/10.1080/1025584031000097933

Fluent, A.N.S.Y.S. (2011). *Ansys fluent theory guide* (pp. 724–746). Ansys Inc.

Gholampour, S. (2018). FSI simulation of CSF hydrodynamic changes in a large population of non-communicating hydrocephalus patients during treatment process with regard to their clinical symptoms. *PloS One*, *13*(4), e0196216–e0196216. https://doi.org/10.1371/journal.pone.0196216

Holmlund, P. (2019). Fluid dynamic principles for analysis of intracranial pressure control: application towards space medicine and hydrocephalus [PhD dissertation]. Umeå Universitet.

Howden, L., Giddings, D., Power, H., Aroussi, A., Vloeberghs, M., Garnett, M., & Walker, D. (2008). Three-dimensional cerebrospinal fluid flow within the human ventricular system. *Computer Methods in Biomechanics and Biomedical Engineering*, *11*(2), 123–133. https://doi.org/10.1080/10255840701492118

Hydrocephalus Association. (2021). 20 Powerful facts about hydrocephalus. https://www.hydroassoc.org/powerful-facts/

Jacobson, E. E., Fletcher, D. F., Morgan, M. K., & Johnston, I. H. (1996). Fluid dynamics of the cerebral aqueduct. *Pediatric Neurosurgery*, *24*(5), 229. https://go.exlibris.link/D8tQW9t1

Jacobson, E. E., Fletcher, D. F., Morgan, M. K., & Johnston, I. H. (1999). Computer modelling of the cerebrospinal fluid flow dynamics of aqueduct stenosis. *Medical & Biological Engineering & Computing*, *37*(1), 59–63. https://doi.org/10.1007/BF02513267

Koombua, K., Pidaparti, R. M., Longest, P. W., & Ward, K. R. (2008). Computational analysis of fluid characteristics in rigid and flexible human respiratory airway models.

Engineering Applications of Computational Fluid Mechanics, *2*(2), 185–194. https://doi.org/10.1080/19942060.2008.11015220

Kurtcuoglu, V., Poulikakos, D., & Ventikos, Y. (2005). Computational modeling of the mechanical behavior of the cerebrospinal fluid system. *Journal of Biomechanical Engineering*, *127*(2), 264. https://go.exlibris.link/BQxPDLvF

Lee, J. H., Lee, H. K., Kim, J. K., Kim, H. J., Park, J. K., & Choi, C. G. (2004). CSF flow quantification of the cerebral aqueduct in normal volunteers using phase contrast cine MR imaging. *Korean Journal of Radiology*, *5*(2), 1–86. https://doi.org/10.3348/kjr.2004.5.2.81

Linninger, A. A., Tsakiris, C., Zhu, D. C., Xenos, M., Roycewicz, P., Danziger, Z., & Penn, R. (2005). Pulsatile cerebrospinal fluid dynamics in the human brain. *IEEE Transactions on Biomedical Engineering*, *52*(4), 557–565. https://doi.org/10.1109/TBME.2005.844021

Masoumi, N., Bastani, D., Najarian, S., Ganji, F., Farmanzad, F., & Seddighi, A. S. (2010). Mathematical modeling of CSF pulsatile hydrodynamics based on fluid-solid interaction. *IEEE Transactions on Biomedical Engineering*, *57*(6), 1255–1263. https://doi.org/10.1109/TBME.2009.2037975

Murphy, H., Jaafari, H., & Dobrovolny, H. M. (2016). Differences in predictions of ODE models of tumor growth: A cautionary example. *BMC Cancer*, *16*(161), 163–163. https://doi.org/10.1186/s12885-016-2164-x

Šutalo, I. D., Bui, A. V., Ahmed, S., Liffman, K., & Manasseh, R. (2014). Modeling of flow through the circle of Willis and cerebral vasculature to assess the effects of changes in the peripheral small cerebral vasculature on the inflows. *Engineering Applications of Computational Fluid Mechanics*, *8*(4), 609–622. https://doi.org/10.1080/19942060.2014.11083311

Sweetman, B., & Linninger, A. A. (2011). Cerebrospinal fluid flow dynamics in the central nervous system. *Annals of Biomedical Engineering*, *39*(1), 484–496. https://doi.org/10.1007/s10439-010-0141-0

Takizawa, K., Matsumae, M., Sunohara, S., Yatsushiro, S., & Kuroda, K. (2017). Characterization of cardiac-and respiratory-driven cerebrospinal fluid motion based on asynchronous phase-contrast magnetic resonance imaging in volunteers. *Fluids and Barriers of the CNS*, *14*(1), 1–8. https://doi.org/10.1186/s12987-016-0048-8

Tu, J., Yeoh, G. H., & Liu, C. (2018). *Computational fluid dynamics: A practical approach*. Butterworth-Heinemann.

Wagshul, M. E., Chen, J. J., Egnor, M. R., McCormack, E. J., & Roche, P. E. (2006). Amplitude and phase of cerebrospinal fluid pulsations: Experimental studies and review of the literature. *Journal of Neurosurgery*, *104*(5), 810–819. https://doi.org/10.3171/jns.2006.104.5.810

Yang, B., Tse, K.-M., Chen, N., Tan, L.-B., Zheng, Q.-Q., Yang, H.-M., Hu, M., Pan, G., & Lee, H.-P. (2014). Development of a finite element head model for the study of impact head injury. *BioMed Research International*, *2014*, 1–14. https://doi.org/10.1155/2014/408278